

# Gradual unlocking of plate boundary controlled initiation of the 2014 Iquique earthquake

Bernd Schurr<sup>1</sup>, Günter Asch<sup>1</sup>, Sebastian Hainzl<sup>1</sup>, Jonathan Bedford<sup>1</sup>, Andreas Hoechner<sup>1</sup>, Mauro Palo<sup>1</sup>, Rongjiang Wang<sup>1</sup>, Marcos Moreno<sup>1</sup>, Mitja Bartsch<sup>1</sup>, Yong Zhang<sup>2</sup>, Onno Oncken<sup>1</sup>, Frederik Tilmann<sup>1</sup>, Torsten Dahm<sup>1</sup>, Pia Victor<sup>1</sup>, Sergio Barrientos<sup>3</sup> & Jean-Pierre Vilotte<sup>4</sup>

On 1 April 2014, Northern Chile was struck by a magnitude 8.1 earthquake following a protracted series of foreshocks. The Integrated Plate Boundary Observatory Chile monitored the entire sequence of events, providing unprecedented resolution of the build-up to the main event and its rupture evolution. Here we show that the Iquique earthquake broke a central fraction of the so-called northern Chile seismic gap, the last major segment of the South American plate boundary that had not ruptured in the past century<sup>1,2</sup>. Since July 2013 three seismic clusters, each lasting a few weeks, hit this part of the plate boundary with earthquakes of increasing peak magnitudes. Starting with the second cluster, geodetic observations show surface displacements that can be associated with slip on the plate interface. These seismic clusters and their slip transients occupied a part of the plate interface that was transitional between a fully locked and a creeping portion. Leading up to this earthquake, the *b* value of the foreshocks gradually decreased during the years before the earthquake, reversing its trend a few days before the Iquique earthquake. The mainshock finally nucleated at the northern end of the foreshock area, which skirted a locked patch, and ruptured mainly downdip towards higher locking. Peak slip was attained immediately downdip of the foreshock region and at the margin of the locked patch. We conclude that gradual weakening of the central part of the seismic gap accentuated by the foreshock activity in a zone of intermediate seismic coupling was instrumental in causing final failure, distinguishing the Iquique earthquake from most great earthquakes. Finally, only one-third of the gap was broken and the remaining locked segments now pose a significant, increased seismic hazard with the potential to host an earthquake with a magnitude of >8.5.

The northern Chile–southern Peru seismic gap last broke in 1877 in a great earthquake ( $M_w \sim 8.8$ )<sup>1</sup> that ruptured from south of Arica to the Mejillones peninsula (see Fig. 1). The reported historical recurrence interval for the past 500 years in this region has been estimated at  $111 \pm 33$  years<sup>1</sup>, making it probably the most mature seismic gap along the South American plate boundary. In the past two decades the two adjoining segments south and north broke in the  $M_w$  8.1 Antofagasta earthquake of 1995 (refs 3, 4) and the  $M_w$  8.4 Arequipa earthquake of 2001 in southern Peru<sup>5</sup>. In the previous cycle the southern Peru and northern Chile segments broke within few years (Fig. 1), suggesting that they might be coupled in time<sup>1</sup>. The imminence of a large megathrust event in this region motivated the setting up of an international monitoring effort with the Integrated Plate Boundary Observatory Chile (IPOC). Having started in 2007, there now exists an exceptional database that monitors the gradual plate boundary failure with various geophysical techniques.

Several major earthquakes ( $M_w > 7$ ) have occurred in this gap since 1850 (Fig. 1); the largest until now was the  $M_w$  7.7 Tocopilla earthquake in 2007, which broke the southern rim of this segment beneath and north of Mejillones peninsula along a total length of 150 km. Only the downdip end of the locked zone slipped in this event, and the total slip in the

rupture area was less than 2.6 m (refs 6, 7) leaving most of the past slip deficit of  $\sim 8$ –9 m accumulated since 1877 unaffected<sup>8</sup>. On 1 April 2014, the  $M_w$  8.1 Iquique earthquake north of Iquique struck the central portion of the gap. Using seismological and geodetic observations we here analyse the rupture, its relationship to previous locking of the plate interface, and the pre-seismic transients leading up to the earthquake.

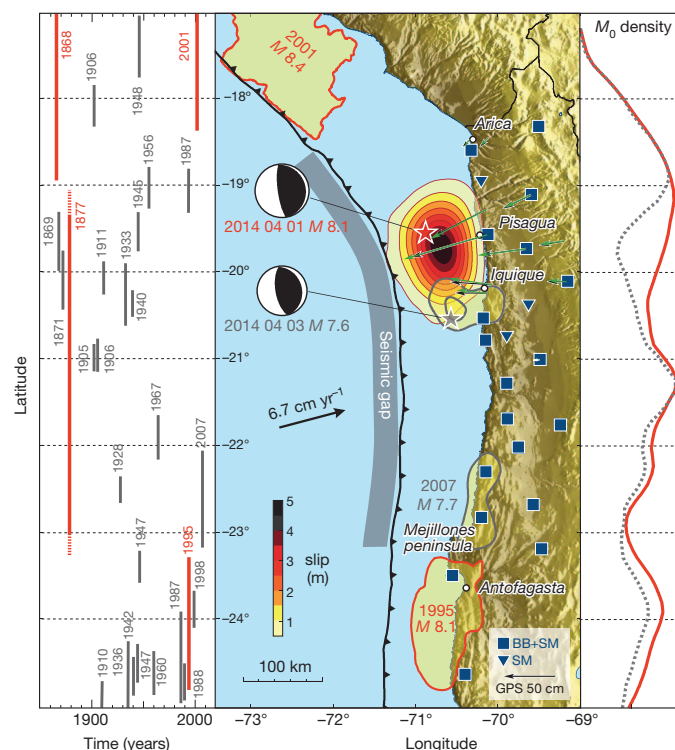


**Figure 1 | Map of Northern Chile and Southern Peru showing historical earthquakes and instrumentally recorded megathrust ruptures.** IPOC instruments used in the present study (BB, broadband; SM, strong motion) are shown as blue symbols. Left: historical<sup>1,2</sup> and instrumental earthquake record. Centre: rupture length was calculated using the regression suggested in ref. 28, with grey lines for earthquakes  $M > 7$  and red lines for  $M_w > 8$ . The slip distribution of the 2014 Iquique event and its largest aftershock derived in this study are colour coded, with contour intervals of 0.5 m. The green and black vectors are the observed and modelled horizontal surface displacements of the mainshock. The slip areas of the most recent other large ruptures<sup>4,5,7</sup> are also plotted. Right: moment deficit per kilometre along strike left along the plate boundary after the Iquique event for moment accumulated since 1877, assuming current locking (Fig. 3a). The total accumulated moment since 1877 from  $17^\circ$  S to  $25^\circ$  S (red solid line) is 8.97; the remaining moment after subtracting all earthquake events with  $M_w > 7$  (grey dotted line) is 8.91 for the entire northern Chile–southern Peru seismic gap.

<sup>1</sup>GFZ Helmholtz Centre Potsdam, German Research Centre for Geosciences, Telegrafenberg, 14473 Potsdam, Germany. <sup>2</sup>School of Earth and Space Sciences, Peking University, Beijing 100871, China. <sup>3</sup>Centro Sismológico Nacional, Universidad de Chile, Facultad de Ciencias Físicas y Matemáticas, Blanco Encalada 2002, Santiago, Chile. <sup>4</sup>Institut de Physique du Globe de Paris, 1, rue Jussieu, 75238 Paris cedex 05, France.

Kinematic analysis of the  $M_w$  8.1 Iquique rupture makes use of two complementary approaches. First, we performed waveform modelling of local strong motion seismograms and teleseismic body waves to constrain the kinematic development of the rupture towards the final displacements in a joint inversion with continuous GPS data of static displacements (Figs 1 and 2a). Second, we used the backprojection technique applied to stations in North America to map the radiation of high-frequency seismic waves (HFSR; 1–4 Hz)<sup>9,10</sup>. The latter technique is not sensitive to absolute slip amplitudes, but rather to changes in slip and rupture velocity. During the first 35–40 s the rupture propagated downdip with increasing velocity, nearly reaching the coastline (Fig. 2a, b). Towards the end of the rupture, the area near the epicentre was reactivated. In spite of the relatively complicated kinematic history of the rupture, the cumulative slip shows a simple ‘bullseye’ pattern with a peak co-seismic slip of about 4.4 m (Fig. 1), consistent with the slip model in ref. 11 based on teleseismic and deep-water tsunami wave recordings. A slip patch of similar size and magnitude has been found<sup>12</sup> but with the highest slip placed ~40 km further south from teleseismic-only recordings; however, this seems not to be compatible with onshore displacement measurements from GPS. The largest aftershock so far was the  $M_w$  7.6 event of 3 April that, like the mainshock, ruptured initially downdip. Rupture then propagated northeastwards, attaining a peak slip of 1.2 m after about 20 s. Both earthquakes broke a total of 200 km of the margin.

The Iquique rupture affected an area shown from geodetic analysis to be a zone of intermediate interseismic coupling at 18.5°–21° S interrupting the otherwise fully locked northern Chile–southern Peru gap<sup>8,13</sup> (Fig. 3a). The Iquique mainshock nucleated at the northwestern border of a locked patch and ruptured towards its centre (Figs 2a and 3a). The downdip end of the mainshock and for the large  $M_w$  7.6 aftershock rupture

mapped by both the HFSR and co-seismic slip agrees quite accurately with the downdip end interseismic coupling (Figs 2a, c and 3a). The accelerated downdip rupture propagation for both earthquakes closely followed the gradient towards higher locking. The Iquique event and its largest aftershock therefore seem to have broken the central, only partly locked segment of the northern Chile–southern Peru seismic gap, releasing part of the slip deficit accumulated here since 1877 (compare Fig. 1).

The seismicity before the Iquique earthquake also concentrated in this zone of intermediate locking at the fringe of the highly locked, high-slip patch (Fig. 3a). Starting in July 2013, three foreshock clusters with increasingly larger peak magnitudes and cumulative seismic moment occurred here (Figs 2c and 3a, c). The mainshock rupture started at the northern end of the foreshock zone, inside the region of intermediate locking (Figs 2c and 3a). The second foreshock cluster (January 2014) is associated with a weak transient deformation, whereas the third cluster (March 2014) shows a very distinct transient signal. GPS displacement vectors calculated over the times spanning these foreshock clusters point towards the cluster epicentres (Extended Data Fig. 4). Deformation for both transients is entirely explained by the cumulative co-seismic displacement of the respective foreshock clusters (Fig. 3d inset and Extended Data Fig. 4). The area affected by the foreshocks is then reactivated by the aftershock sequence of the Iquique earthquake (Fig. 2c). Comparing this with the long-term deformation history of the margin, we found that the same area shows a high gradient of locking from weakly locked updip to fully locked downdip (Fig. 3a).

Additionally, the analysis of the frequency–magnitude distribution of the foreshocks reveals outstanding characteristics in both the spatial and temporal vicinities of the rupture. The earthquake number  $N$  as a function of the magnitude  $M$  is found to follow the well-known Gutenberg–Richter

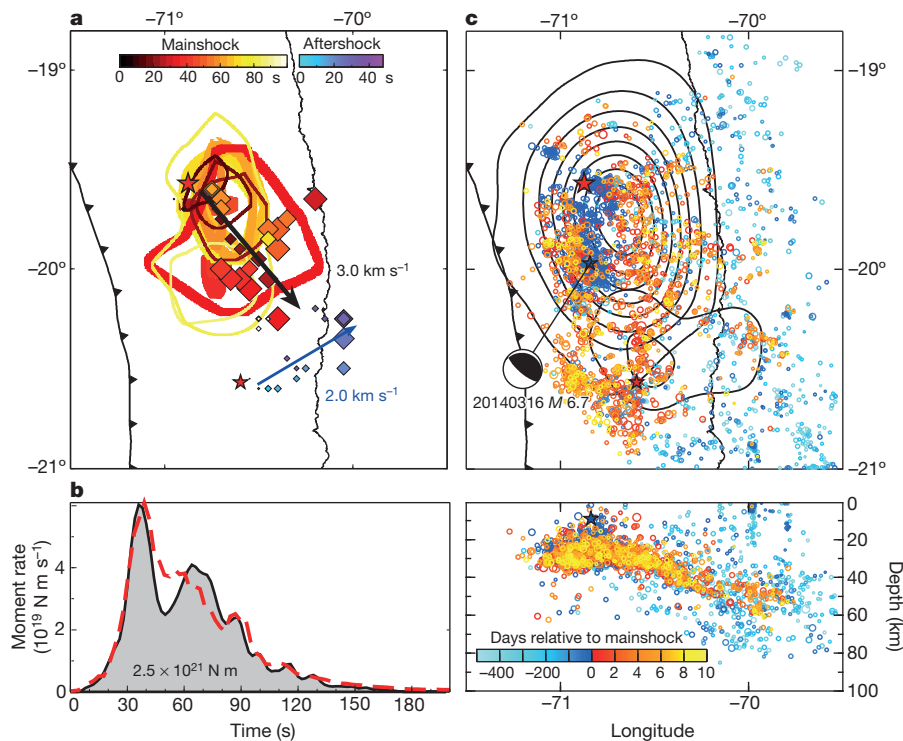


**Figure 2 | Kinematic rupture development of the  $M_w$  8.1 main and  $M_w$  7.6 aftershock and the distribution of foreshocks and aftershocks.** The nucleation point of each earthquake rupture is indicated by a coloured star. **a**, Arrows indicate the propagation of main energy release during the first 40 and 25 s for mainshock and aftershock, respectively. The contour lines represent isolines of slip rate for the mainshock from the kinematic inversion during different time intervals after rupture nucleation (0.05 m s<sup>-1</sup> intervals, line thickness scaled by slip-rate). Coloured diamonds represent maxima of semblance scaled to the peak value of the emitted energy for mainshock and aftershock for each time step based on the backprojection of teleseismic

waveforms. **b**, Moment rate and time history of backprojected energy (arbitrary absolute scale). Black solid line, mainshock kinematic source-time-function; red dashed line, rescaled backprojection energy. **c**, Map (top) and longitudinal cross-section (bottom) of ~3,600 foreshocks and ~1,400 aftershocks coloured according to their time of occurrence relative to the mainshock. The slips of the mainshock and largest aftershock are contoured. The beachball depicts the double-couple of the largest  $M_w$  6.7 foreshock that had a rupture geometry distinctively different from the mainshock and largest aftershock (Fig. 1) and a centroid depth of only 9 km (blue star) and that thus probably occurred in the upper plate.

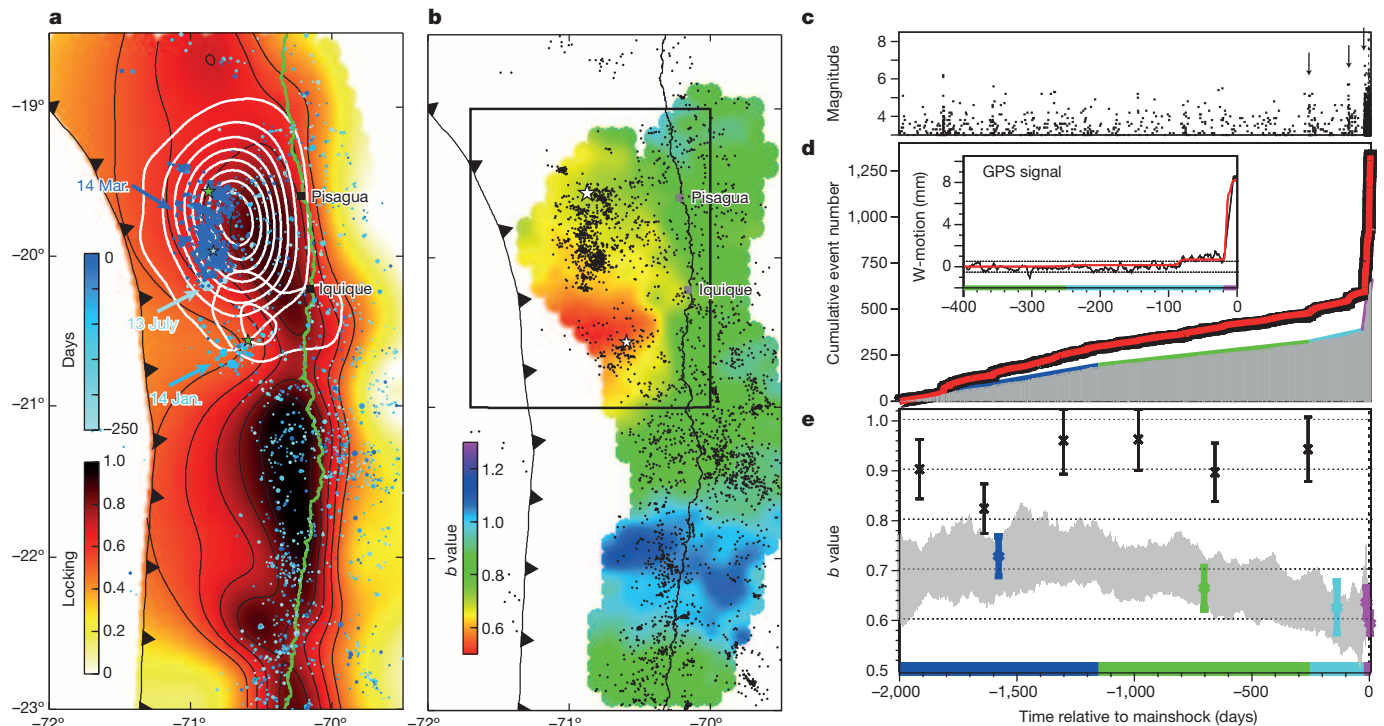


**Figure 3 | Maps of interseismic locking and  $b$  value, and time history of seismicity and deformation.** **a**, Geodetic interseismic locking and foreshocks. The July–August 2013, January and March 2014 foreshock clusters are marked. **b**,  $b$ -value map of the central portion of northern Chile gap for the last 2000 days before the mainshock, where results are calculated for all  $M \geq 3$  foreshocks within 50 km if their number exceeds 100. The rectangular box encloses the area used for the results in **c–e**. **c**, Magnitude–time plot. Arrows mark the July–August 2013, January and March 2014 clusters. **d**, Observed (black thick line) and ETAS-modelled (red line) cumulative  $M \geq 3$  activity; the thin coloured

lines are fits of the estimated background (grey shaded area) for the four phases, during each of which the background rate is almost constant (see the text). The inset shows measured GPS displacement time-series stacked from near-coast stations between  $19^\circ$  S and  $21^\circ$  S smoothed with a four-day moving average and the modelled signal related to cumulative slip of the foreshock events. **e**, Time series of  $b$  value (means  $\pm$  s.d.) for the events inside the box (coloured and grey shaded area). Black points and bars refer to the results for the events outside the box.

relation,  $N \approx 10^{-bM}$ .  $b$  values have been proposed to act as a stress sensor, with low  $b$  values indicating high stresses<sup>14</sup>. Mapping the  $b$  value in Fig. 3b indicates significantly lower  $b$  values in the source area than in all other regions where the  $b$  value can be resolved. A gradual decrease in the  $b$  value from about 0.75 to below 0.6 is observed in the source region within the three years before the Iquique earthquake (Fig. 3e). This only reverses within the last days of the foreshock sequence. Similar decreases in  $b$  values before large megathrust earthquakes have recently been documented, in particular for the  $M$  9 Tohoku event<sup>15</sup>.

To reveal potential changes of background seismic activity related to aseismic processes, we fit the foreshock seismicity by means of an Epidemic-Type-Aftershock-Sequence (ETAS) model<sup>16</sup>, identifying only 42% of pre-mainshock events as Omori-type aftershocks triggered by larger foreshocks. Using the Akaike information criterion<sup>17</sup>, the remaining background rate is found to be significantly time dependent: we identified four subsequent periods of almost constant background rates (Fig. 3d, e). The mainshock preparation process seems to have been initiated by a relative seismic quiescence, which starts at the same time as  $b$  values are found to drop and ends in July 2013, when the background rate returns to approximately the pre-quiescence values; the final phase starts 18 days before the quake, when the background seismicity increases more than 35-fold in conjunction with the onset of the final transient GPS signal.

Such a sequence of seismic quiescence, recovery and acceleration of background activity is expected in the stress accumulation framework<sup>18</sup>. On the basis of the inverted ETAS parameters and the low  $b$  values before the mainshock, the seismicity is expected to accelerate with time as the result of a branching ratio—that is, the average number of daughter events per earthquake—larger than one indicating a transient supercritical state<sup>19</sup>. Hence, the period leading to the Iquique earthquake documents progressive asperity failure, here observed in unprecedented detail. An increase

in foreshock activity preceding subduction megathrust events has repeatedly been reported<sup>18,20,21</sup>. In contrast to, for example, the foreshocks of the 2011  $M$  9 Tohoku–Oki earthquake<sup>21</sup>, which started about three weeks before the mainshock, the foreshock clusters described here have been active since the start of our observations in 2007. However, only more recently have foreshocks with increasing magnitudes and thus more fertile aftershock sequences resulted in a supercritical state with self-accelerating seismicity<sup>19</sup>. This ultimately allowed an earthquake to nucleate that was strong enough to break into the stronger locked and thus aseismic part of the interface. From the spatial correlation of foreshock activity and slip gradients with the Iquique mainshock rupture region, we infer gradual unlocking of the plate interface. Moreover, the start of the decrease in  $b$  value  $\sim 3$  years ago, in spite of constant plate convergence and loading rate, indicates a physical change at the plate interface. From only intermediate locking the Iquique segment seems to have been dominated by mostly smaller locked asperities embedded in a conditionally stable environment, if we assume that rate and state frictional behaviour is controlling locking and creep<sup>22–24</sup>. Progressive rupturing of the smaller asperities by foreshocks will have loaded the remaining larger asperities in this zone until their failure: this evolution may be seen as the culmination of a runaway process as the likely key mechanism leading up to the Iquique earthquake. Both the rupture direction and speed of the mainshock and its triggered large aftershock are controlled by the stress gradient in the remaining asperities, corroborating theoretical analysis<sup>25</sup>. This indicates that not only the size of larger asperities but also their stress topography is important for understanding the propagation, acceleration and stopping of megathrust earthquakes. The Iquique event broke a region of heterogeneous coupling, where rupture not only broke a moderate-sized asperity but also penetrated into a weakly coupled zone, possibly by dynamic weakening<sup>26</sup>.



Earthquake swarms occur preferentially in regions of low interseismic strain accumulation, which tend to delimit subsequent ruptures of plate interface zones<sup>27</sup>. The  $M_w$  7.7 Tocopilla earthquake with its aftershocks and the  $M_w$  8.1 Iquique earthquake with its foreshocks might be considered similar features. They embrace the rims of a highly locked zone 250 km long in the centre of the northern Chile–southern Peru gap with an accumulated slip deficit<sup>8</sup> of some 8–9 m since 1877. Estimating the moment deficit for the entire seismic gap yields the potential for an earthquake with a maximum magnitude of  $M_w \sim 8.9$  (Fig. 1) for the historically less likely case that the entire zone fails in a single event. However, the reduction of the slip deficit by about 50% in the Iquique earthquake area (Fig. 1) decreases the probability that a future earthquake will release the whole remaining slip deficit at once. As the slip deficit reduction is only partial, though, this region will not necessarily act as a barrier: the seismic potential of this area remains high.

**Online Content** Methods, along with any additional Extended Data display items and Source Data, are available in the online version of the paper; references unique to these sections appear only in the online paper.

**Received 23 May; accepted 14 July 2014.**

**Published online 13 August 2014.**

- Comte, D. & Pardo, M. Reappraisal of great historical earthquakes in the northern Chile and southern Peru seismic gaps. *Nat. Hazards* **4**, 23–44 (1991).
- Chlieh, M. *et al.* Interseismic coupling and seismic potential along the Central Andes subduction zone. *J. Geophys. Res.* **116**, 1–21 (2011).
- Ruegg, J. C. *et al.* The  $M_w = 8.1$  Antofagasta (North Chile) Earthquake of July 30, 1995: first results from teleseismic and geodetic data. *Geophys. Res. Lett.* **23**, 917–920 (1996).
- Chlieh, M. *et al.* Crustal deformation and fault slip during the seismic cycle in the North Chile subduction zone, from GPS and InSAR observations. *Geophys. J. Int.* **158**, 695–711 (2004).
- Pritchard, M. E. *et al.* Geodetic, teleseismic, and strong motion constraints on slip from recent southern Peru subduction zone earthquakes. *J. Geophys. Res.* **112**, 1–24 (2007).
- Delouis, B., Pardo, M., Legrand, D. & Monfret, T. The  $M_w$  7.7 Tocopilla earthquake of 14 November 2007 at the southern edge of the northern Chile seismic gap: rupture in the deep part of the coupled plate interface. *Bull. Seismol. Soc. Am.* **99**, 87–94 (2009).
- Schurr, B. *et al.* The 2007  $M_w$  7.7 Tocopilla northern Chile earthquake sequence: Implications for along-strike and downdip rupture segmentation and megathrust frictional behavior. *J. Geophys. Res.* **117**, 1–19 (2012).
- Métis, M. *et al.* Revisiting the North Chile seismic gap segmentation using GPS-derived interseismic coupling. *Geophys. J. Int.* **194**, 1283–1294 (2013).
- Krüger, F. & Ohrnberger, M. Tracking the rupture of the  $M_w = 9.3$  Sumatra earthquake over 1,150 km at teleseismic distance. *Nature* **435**, 937–939 (2005).
- Rössler, D., Krüger, F., Ohrnberger, M. & Ehlert, L. Rapid characterisation of large earthquakes by multiple seismic broadband arrays. *Nat. Hazards Earth Syst. Sci.* **10**, 923–932 (2010).
- Lay, T., Yue, H., Brodsky, E. E. & An, C. The 1 April 2014 Iquique, Chile,  $M_w$  8.1 earthquake rupture sequence. *Geophys. Res. Lett.* **41**, 3818–3825 (2014).
- Yagi, Y. *et al.* Rupture process of the 2014 Iquique Chile Earthquake in relation with the foreshock activity. *Geophys. Res. Lett.* **41**, 1–6 (2014).
- Béjar-Pizarro, M. *et al.* Andean structural control on interseismic coupling in the North Chile subduction zone. *Nature Geosci.* **6**, 462–467 (2013).
- Schorlemmer, D., Wiemer, S. & Wyss, M. Variations in earthquake-size distribution across different stress regimes. *Nature* **437**, 539–542 (2005).
- Nanjo, K. Z., Hirata, N., Obara, K. & Kasahara, K. Decade-scale decrease in  $b$  value prior to the  $M_9$ -class 2011 Tohoku and 2004 Sumatra quakes. *Geophys. Res. Lett.* **39**, L20304 (2012).
- Ogata, Y. Statistical models for earthquake occurrences and residual analysis for point processes. *J. Am. Stat. Assoc.* **83**, 9–27 (1988).
- Marsan, D., Prono, E. & Helmstetter, A. Monitoring aseismic forcing in fault zones using earthquake time series. *Bull. Seismol. Soc. Am.* **103**, 169–179 (2013).
- Mignan, A. Seismicity precursors to large earthquakes unified in a stress accumulation framework. *Geophys. Res. Lett.* **39**, L21308 (2012).
- Helmstetter, A., Kagan, Y. Y. & Jackson, D. D. Importance of small earthquakes for stress transfers and earthquake triggering. *J. Geophys. Res.* **110**, 1–13 (2005).
- Bouchon, M., Durand, V., Marsan, D., Karabulut, H. & Schmittbuhl, J. The long precursory phase of most large interplate earthquakes. *Nature Geosci.* **6**, 299–302 (2013).
- Kato, A. *et al.* Propagation of slow slip leading up to the 2011  $M_w$  9.0 Tohoku-Oki earthquake. *Science* **335**, 705–708 (2012).
- Scholz, C. H. Earthquakes and friction laws. *Nature* **391**, 37–42 (1998).
- Bilek, S. L. & Lay, T. Tsunami earthquakes possibly widespread manifestations of frictional conditional stability. *Geophys. Res. Lett.* **29**, 1–4 (2002).
- Kaneko, Y., Avouac, J. P. & Lapusta, N. Towards inferring earthquake patterns from geodetic observations of interseismic coupling. *Nature Geosci.* **3**, 363–369 (2010).
- Das, S. & Kostrov, B. V. Breaking of a single asperity: rupture process and seismic radiation. *J. Geophys. Res.* **88**, 4277–4288 (1983).
- Noda, H. & Lapusta, N. Stable creeping fault segments can become destructive as a result of dynamic weakening. *Nature* **493**, 518–521 (2013).
- Holtkamp, S. & Brudzinski, M. R. Megathrust earthquake swarms indicate frictional changes which delimit large earthquake ruptures. *Earth Planet. Sci. Lett.* **390**, 234–243 (2014).
- Dorbath, L., Cisternas, A. & Dorbath, C. Assessment of the size of large and great historical earthquakes in Peru. *Bull. Seismol. Soc. Am.* **80**, 551–576 (1990).

**Supplementary Information** is available in the online version of the paper.

**Acknowledgements** Data used in this study come from the IPOC initiative (<http://www.ipoc-network.org>) operated by the GFZ – German Research Centre for Geosciences, Institut de Physique du Globe de Paris, Centro Sismológico Nacional, Universidad de Chile, and Universidad Católica del Norte, Antofagasta, Chile. We also acknowledge the French–Chilean International Associated Laboratory (LIA) ‘Montessus de Ballore’ and the USA–Chilean Central Andean Tectonic Observatory Geodetic Array projects for giving access to data of several of their continuous GPS (cGPS) stations in Chile. Part of this work was made possible by the Hazard Assessment and Risk Team (HART) initiative funded by the GFZ and Hannover Re.

**Author Contributions** B.S. processed the entire seismicity of the IPOC network set up by G.A., S.B., J.-P.V. and B.S. S.H. performed the ETAS and  $b$ -value analysis. R.W., Y.Z. and T.D. contributed the co-seismic slip models. M.P. and F.T. performed the backprojection analysis. M.B. was responsible for the GPS data processing. J.B., A.H. and M.M. analysed geodetic locking and slip transients. A.H. modelled the accumulated, released and remaining moment. P.V. compiled the historical earthquake record, and O.O. wrote major parts of the mechanical interpretation.

**Author Information** Reprints and permissions information is available at [www.nature.com/reprints](http://www.nature.com/reprints). The authors declare no competing financial interests. Readers are welcome to comment on the online version of the paper. Correspondence and requests for materials should be addressed to B.S. ([schurr@gfz-potsdam.de](mailto:schurr@gfz-potsdam.de)).

## METHODS

**Kinematic source inversion.** Kinematic slip inversions were made for the  $M_w$  8.1 mainshock on 1 April and the  $M_w$  7.6 aftershock on 3 April. For each earthquake we first inverted the static three-component GPS displacement data for the final fault slip and then teleseismic and local strong-motion waveforms for the time-dependent kinematic rupture process. Finally we performed a joint inversion of the waveform and GPS data.

The teleseismic data (P waveforms on the vertical component) were selected from a set of broadband stations (18 for the mainshock and 17 for the aftershock) with a good azimuth and distance coverage (see Extended Data Fig. 1c). In addition, seismograms from 20 three-component strong-motion seismographs were used. Both teleseismic and local waveform data were converted to velocity and filtered with a 0.01–0.1-Hz bandpass. The static displacement data were gleaned from 21 continuous GPS stations, most of which are co-located with the strong-motion stations. In the joint inversions, the GPS and seismic waveform data sets were weighted equally.

For the inversion we used a linear approach implemented in ref. 29, in which multiple time windows are used for describing the sub-fault source time functions. The fault geometry for the two earthquakes was adopted from the Slab1.0 model<sup>30</sup>. The sub-fault size ranges between 10 and 15 km. Synthetic Green's functions were calculated with the code of Wang<sup>31</sup> based on the seismic reference Earth model AK135 (ref. 32) modified with the local one-dimensional crust structure from the CRUST 2.0 model<sup>33</sup>.

Extended Data Fig. 1a shows the final slip distribution for the mainshock of 1 April, which is characterized by a single asperity with the lower edge just below the coastline. This result is robust, showing similar slip distribution with and without the constraint from the static GPS displacement data. However, the temporal development of the rupture features two sub-events, as shown by Supplementary Video 1. The rupture was initiated in the foreshock region (Figs 2 and 3) and propagated in the south-down-dip direction along the maximum locking gradient during the first 40–50 s (first peak in source-time-function (STF)). Then the region near the hypocentre became reactivated and the rupture propagated towards the north-down-dip and up-dip directions simultaneously (second peak in STF). The observed and modelled teleseismic and strong-motion seismograms are shown in Extended Data Fig. 1c.

Similarly, Extended Data Fig. 1b and Supplementary Video 2 show the kinematic results for the aftershock of 3 April. This aftershock extended the mainshock rupture further in the southeast-down-dip direction and crossed the coastline near the city of Iquique. Its slip distribution is rather compact, despite a quite complicated STF. **Backprojection.** In the backprojection analysis, the source position of the seismic radiation is inferred by projecting the seismic wavefront of ground velocity recorded by an array of stations at teleseismic distances onto the source region<sup>9,34</sup>. The source location is chosen as the area in the source region leading to the best overlap between the traces.

We have backprojected the radiation emitted in the frequency band 1–4 Hz (filtered by a zero-phase fourth-order Butterworth filter) dividing the rupture process in time windows of 8 s, sliding with an overlap of 6 s. We have used stations from the continental USA (mostly from the TA and N4 networks (<http://www.usarray.org>)) and have searched the source over a grid in the range 18°–21° S and 69°–71° W with a spacing of 0.05°.

We have measured the coherence between the traces by semblance<sup>10,35</sup>, which is a normalized version of the stacked energy and ranges in the interval 0–1, where  $S = 1$  signifies perfectly coherent signals. Semblance and energy at the  $i$ th grid point in the source area are defined as follows:

$$S_i(t) = \frac{1}{N} \frac{\int_{-L/2}^{L/2} \left| \sum_{k=1}^N \bar{u}_k(t - t_{ik} - t') \right|^2 dt'}{\int_{-L/2}^{L/2} \sum_{k=1}^N \bar{u}_k(t - t_{ik} - t') dt'}$$

$$E_i(t) = \frac{1}{N} \int_{-L/2}^{L/2} \left| \sum_{k=1}^N u_k(t - t_{ik} - t') \right|^2 dt'$$

where  $u_k(t)$  is the continuous trace of the  $k$ th station, and  $\bar{u}_k(t)$  is the continuous trace normalized to its maximum absolute value during each time window,  $N$  is the number of sensors,  $t_{ik}$  is the travel time from the  $i$ th grid cell to the  $k$ th station, and the time integral is over the analysis window ( $L$ ).

The travel times are those predicted by a one-dimensional global velocity model plus a site-based correction:

$$t_{ik} = t_{ik}^{\text{1D}} + \Delta t_k^s$$

where  $t_{ik}^{\text{1D}}$  is the travel time from the  $i$ th grid point to the  $k$ th sensor predicted by the ak135 velocity model<sup>32</sup> and  $\Delta t_k^s$  is a static correction associated with each station.

$\Delta t_k^s$  has been estimated as the mean value of the residual time shifts between one station and all the others after removal of the travel times predicted by the one-dimensional model between each station and the hypocentre provided by GEOFON (70.82° S, 19.64° W). The residual time shifts between the stations have been calculated maximizing the cross-correlation of the first 8 s of the mainshock (filtered in the band 0.4–3 Hz) between all the possible station pairs. Only stations with mean cross-correlation higher than 0.8 have been selected, leading to a set of 310 stations adopted for the backprojection analysis. The same set of static corrections has been adopted for both the mainshock and the aftershock.

The time development of semblance and energy is shown in Extended Data Fig. 2a, b. Supplementary Videos 3 and 4 give an impression of the propagation of rupture energy. In Extended Data Fig. 2c we quantify the rupture speed along a down-dip profile on the rupture plane.

**Interseismic locking.** Although models of interseismic coupling for this region exist<sup>2,8,13</sup>, it is in the interest of consistency to produce a locking model on the same geometry as used for the co-seismic slip modelling. We took the ITRF08 GPS velocities data of ref. 8 and performed our own corrections to fix velocities to a stable South American reference frame, and to correct for overlapping tectonic signals of shortening and sliver motion.

The GPS velocities in this region are not ready to use in the inversion because they are contaminated by the Andean sliver motion<sup>2</sup> and shortening<sup>36,37</sup>. Previously the velocities were decontaminated by applying a single Euler pole correction on the craton-fixed velocity field<sup>8</sup>. In a similar approach, we applied a series of Euler pole corrections in the following way. First we translated the ITRF08 velocities of ref. 8 into a stable South American reference frame by inverting for the Euler of the rotation of several South American reference stations and applying this Euler pole rotation correction (29.9° S, 115.9° W,  $-0.12^\circ \text{ Myr}^{-1}$ ) to the ITRF08 velocities. Next we applied a correction for the forearc sliver motion by means of another Euler pole correction. The Euler pole for sliver correction (2.4° S, 80.3° W,  $-0.16^\circ \text{ Myr}^{-1}$ ) was calculated from the misfits between data and modelled displacements for a smooth backslip model fully locked from the trench to the coastline. This sliver correction was applied to all the stations in the network. Finally, shortening corrections were applied to the data at selected stations where the misfit between the highly smoothed locked model displacements and the sliver-corrected data was highest. Shortening corrections for stations in the northeast of our model were rotated about an Euler pole of 14.9° S, 72.4° W at  $0.50^\circ \text{ Myr}^{-1}$ . Shortening corrections for stations in the south of our model were rotated about an Euler pole of 14.6° S, 79.4° W at  $0.12^\circ \text{ Myr}^{-1}$ . The sliver and shortening corrections are shown in Extended Data Fig. 3a. Interseismic coupling is modelled with the backslip method. In this modelling scheme the surface displacements due to subduction are modelled as dislocations (backslips) on the plate interface, with regions of largest modelled dislocation interpreted as being the most locked regions. For forward modelling we use a layered elastic half space and an IASP Earth model<sup>38</sup>. The Green's functions are computed using code PSGRN/PSCMP<sup>39</sup>, the geometry consists of  $15 \times 90$  rectangular subfaults with an average edge length of about 13 km and follows the depth of Slab1.0 (ref. 30). The inversion is a weighted damped least-squares scheme<sup>40</sup>; data are weighted according to estimated accuracies. The inversion scheme uses steepness as smoothing operator in the design matrix, taking into account the size and centre distance between neighbouring patches to avoid distortion of the solution. The optimal smoothing factor is found based on an L-curve plot as shown in Extended Data Fig. 3c, used as a basis for locking shown in Extended Data Fig. 3d. Checkerboard tests were performed to assess the resolving power of the inversion (Extended Data Fig. 3e). On the basis of the locking map, we computed the accumulated moment since the 1877  $M_w = 8.8$  earthquake, assuming that the locking was constant at the same level as at present (Extended Data Fig. 3b).

**Characterizing transient signals in the data.** The excellent spatial coverage and proximity of the cGPS network near to the mainshock hypocentre enabled us to analyse the kinematics of the plate interface leading up to the mainshock testing for previous slip and its relationship to the foreshocks. To see any transient signals we first detrended the time series (obtained by the processing detailed below) from the long-term constant deformation due to plate convergence, and removed spurious noise. The detrended time series still contain considerable network-correlated noise, particularly since mid-2013. We suppressed this noise by using the common-mode filtering approach<sup>41</sup>, whereby we selected stations distant from the source region and averaged their detrended signals. This signal was subtracted from the detrended time series at our stations of interest. Finally a moving average of 8 days was applied to the data to smooth the remaining spurious fluctuations. Extended Data Fig. 4a shows the stations of interest (closest to the  $M_w = 8.1$  and  $M_w = 7.6$  hypocentres) and the selection of stations used to average the network-correlated noise. Generally the common-mode filter seems to work reasonably well and brings the detrended time series within noise fluctuations back to the detrended line ( $y = 0$ ), but in some cases the filter over-corrects or under-corrects. The filter is better constrained, and therefore performs better for epochs with fuller station coverage.

From the corrected time series (Extended Data Fig. 4b) we can see that transient slip started in early January 2014, although at some stations the amplitude for the beginning of this transient signal is not higher than the background noise amplitude earlier in the signal. Perhaps the most convincing argument that the case of the transient in early January is a real signal is found when we plot the detrended time series with increasing time in plan view (Extended Data Fig. 4c and Supplementary Video 5). The suspected signal is distinct from noise seen earlier than 2014 in that the vectors point towards a common location, as we would expect as a response for a source of slip on the plate interface. Furthermore, the timing of the transient coincides with the 2 January foreshock cluster, and the GPS vectors are pointing towards the location of this cluster. Furthermore, from Supplementary Video 5 we can see that the displacement associated with the early January cluster is permanent: the azimuths of the southern stations vary wildly before this cluster, whereas after the cluster the azimuths consistently point towards the cluster location. From this result one could suggest that the foreshock activity on the plate interface is mechanically related to plate interface slip in the immediate vicinity. However, the temporal smoothing due to the application of a moving-average filter means that one cannot say which process (earthquakes or cGPS transient) starts first, or whether they are coeval. The largest transient signal begins with the onset of the mid-March foreshock cluster and continues until the eventual rupture of the  $M_w = 8.1$  event of 1 April. This second transient is clearly a real signal because of the large signal-to-noise ratio and again because the vectors of the GPS point towards the foreshock cluster region.

Having established these transients, we can test whether they are explained by co-seismic displacements of the foreshocks, or by aseismic slip. Included in Extended Data Fig. 4 and Supplementary Video 5 are the seismic displacements predicted at the GPS stations by forward-modelling the scaling relation-derived slip for each foreshock in the catalogue, and an assumed rake in the direction opposite to plate convergence. For consistency, the seismic predictions have been smoothed with the same time window as for the data. The evolution of seismic displacement in early January closely matches that of the GPS both in pattern and magnitude. The GPS vectors are then interrupted by noise until we reach the second cluster in mid-March. Cumulative GPS data and seismic predictions at the time of the second cluster are also closely matching in magnitude. Considering the uncertainties involved in the seismic displacement predictions and the noise of the GPS, the remarkable similarity in cumulative displacement between data and prediction indicates a scenario of a mostly seismic release of slip on the plate interface leading up to the  $M_w = 8.1$  mainshock.

**Earthquake catalogue production and analysis.** We analysed the earthquake catalogue within latitude  $18.0^\circ$ – $23.0^\circ$  S and longitude  $69.8^\circ$ – $73.0^\circ$  W since 1 January 2007 including the  $M 8.1$  Pisagua earthquake and its first ten days of aftershocks. The catalogue was produced with a multistage automatic procedure applied to stations from the IPOC network and a few additional long-term temporary stations. We used first detections from a short-term versus long-term average ratio (STA/LTA) trigger and a grid search algorithm for event association and preliminary locations, and then used specialized P-phase and S-phase pick algorithms on targeted phase windows for an improved set of phase picks, which were jointly inverted for new hypocentres and station-phase terms with the use of a one-dimensional velocity model developed for the Chilean forearc<sup>42</sup>. At each step, quality checks were performed to weed out spurious picks, wrong associations, and false and badly constrained events. Finally the catalogue was relocated using the double-difference algorithm<sup>43</sup>. The procedure is described in detail in ref. 44. Magnitudes are local magnitudes ( $M_L$ ) using a standard attenuation relation for California.  $M_L$  calculated in this way has been found to overestimate the size of moderate and larger events in northern Chile for which  $M_w$  is available. The catalogue consists of 16,613 events before and 1,377 events after the mainshock with local magnitudes above 1.2. For our detailed analysis, we focused on a box between latitude  $17.0^\circ$ – $21.0^\circ$  S and longitude  $70.0^\circ$ – $72.0^\circ$  W enclosing the source region of the mainshock, with 3,187  $M > 1.2$  foreshocks and 1,284  $M > 1.4$  aftershocks (available as Source Data). The corresponding magnitude distributions are shown in Extended Data Fig. 5.

Earthquake catalogues are known to be incomplete as regards small magnitudes, in particular directly after large earthquakes<sup>45</sup>. To avoid effects of incomplete detections, we used a cutoff magnitude of  $M_c 3$  which is—to be conservative—well above the completeness value of 2.6 estimated by the maximum curvature method inside the box<sup>46</sup>. For the  $b$ -value map shown in Fig. 3b, we calculated  $b$  values only on grid nodes where the completeness estimator yielded a value  $\leq 3$ . However, after larger earthquakes, catalogues are generally also lacking  $M > M_c$  events for a short time, because the mainshock coda and overlapping aftershocks limit the detection ability. The period with incomplete detection is a function of the mainshock magnitude  $M$  and the cutoff magnitude  $M_c$  and has been found to be well fitted by the functional form  $\log_{10}(\Delta t) = (M - M_c - c_1)/c_2$  in a similar manner to California seismicity<sup>47</sup>, but with slightly different parameters ( $c_1 = 5.2$  and  $c_2 = 1.5$ ). We ignored those incomplete periods in our analysis of  $b$  values as well as in the ETAS modelling.

The corresponding frequency–magnitude distributions are shown by bold lines in Extended Data Fig. 5a.

The  $b$  values are calculated by the maximum-likelihood method according to

$$b = \frac{1}{\ln(10)[\bar{m} - M_c - \Delta M/2]}$$

with  $\bar{m}$  being the mean magnitude and  $\Delta M$  the bin width of the magnitudes in the catalogue (0.1 in our case)<sup>48</sup>, and the standard deviation of the  $b$ -value estimation is calculated according to ref. 49. The results are shown in Fig. 3e. In Extended Data Fig. 5b we additionally present the corresponding frequency–magnitude distributions at different times. Note that the time refers to the average time of 200 subsequent events.

The ETAS model is also fitted by a maximum-likelihood method, in which we applied a method to estimate transient background rates developed recently in ref. 17 and further tested in ref. 50. Earthquake catalogues are usually dominated by aftershock activity, which hinders the detection of changes of background activity related to aseismic processes. Thus we try to decluster the earthquake catalogue to recover this forcing signal. The method is based on the inversion of the empirical ETAS model in which the earthquake  $R$  is determined by summing a background rate  $\mu$  and ongoing Omori-type aftershock activity from precursory earthquakes,

$$R(t) = \mu(t) + \sum_{t_i < t} K e^{\alpha(M - M_c)} / (c + t - t_i)^p$$

with parameters  $c$  and  $p$  related to the temporal decay and  $K$  and  $\alpha$  to the aftershock productivity relation for empirically observed aftershocks. Whereas the background rate is constant in the original model<sup>16</sup>, it is allowed to vary in time in the new approach to account for aseismic transients. However, smoothing of the background rates in time is crucial to avoid overfitting, where the optimal smoothing is determined by the Akaike information criterion.

Although all  $M \geq 2.5$  earthquakes are used to calculate  $R(t)$ , we optimize the parameters and background rate only for  $M \geq 3$  events in completely recorded time intervals (see above). Furthermore, we start the optimization time window not before 2,000 days before the mainshock to minimize the effect of missing historic activity. Our approach yields the aftershock parameters  $c = 0.012$  days,  $P = 1.13$ ,  $K = 0.0048$  and  $\alpha = 1.87$ , which are in the range of typical values observed in previous studies. Depending on the  $b$  value and the maximum magnitude, the branching ratio  $n$ , which is the average number of daughter events per earthquake, can be calculated<sup>19</sup>. Our estimates of  $b$  value show a decrease in  $b$  values from about 0.8 to 0.6 before the mainshock, which corresponds to an increase of the branching ratio from 0.62 and 0.75 to 1.86 and 3.14 for  $M_{\max} = 8.0$  and 9.0, respectively. For  $n < 1$  the system is in a subcritical state where sequences will decay with time. For  $n > 1$  the system is in a supercritical state, where the activity will start to self-accelerate with time; this can obviously be only transient<sup>19</sup>. We find that the source region of the Pisagua earthquake seemed to move gradually from a subcritical into a supercritical state while approaching the mainshock time.

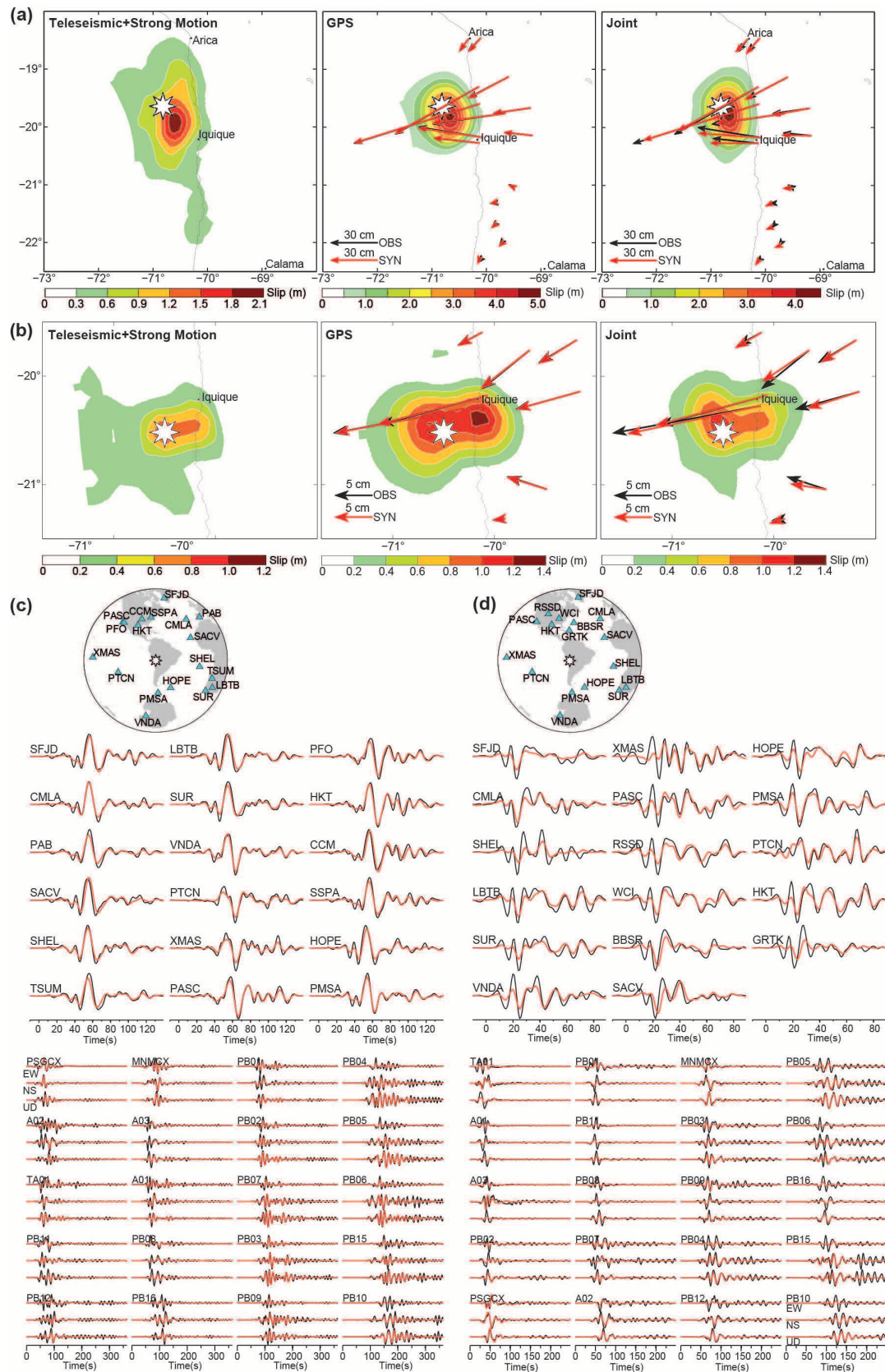
The revealed time-dependent background rate explains about 60% of the observed foreshock activity and can be well fitted by four time periods with constant activity. These periods are characterized by change points at times 1,150, 250 and 18 days before the mainshock, separating an initial phase, a relative quiescence, a recovery phase and a final phase of strong forcing. The corresponding background rates are 0.22  $M \geq 3$  events per day in the period 2,000–1,150 days, 0.14  $M \geq 3$  events per day in the relatively quiet period 1,150–250 days, 0.28  $M \geq 3$  events per day in the period 250–18 days, and 10  $M \geq 3$  events per day in the last 18 days. To determine the significance of these rate changes we calculated the  $Z$  values<sup>51</sup>. We find that all rate changes are significant, with  $|Z| = 4.1, 3.9$  and 12.5 for the changes at 1,150, 250 and 18 days before the mainshock, respectively.

**GNSS data processing strategy.** All processing of GNSS data was done with Bernese GNSS Software version 5.2 (ref. 52). For the preseismic position time series, sites from  $63^\circ$  to  $74^\circ$  W and  $16^\circ$  to  $25^\circ$  S were selected. The processing starts on 1 January 2008 and continues until 20 April 2014. Overall 50 stations are included. Daily solutions are generated using the final satellite orbits and Earth orientation parameters from CODE (Center of Orbit Determination Bern). All parameters are derived from a least-squares adjustment using double-difference phase observations. Both GPS and GLONASS observations were used. Absolute corrections for antenna phase centre offsets and phase centre variations for receivers and satellites<sup>53</sup> associated with the latest realization of the International Terrestrial Reference Frame (ITRF2008) were applied. Ocean loading corrections are derived from ocean tide model FES2004 (ref. 54). An elevation cutoff angle of  $5^\circ$  and a sampling rate of 30 s were used. The dry and wet parts of the troposphere were calculated using the GMF<sup>55</sup>. Whereas the dry part is taken a priori from the model, the wet coefficients are estimated with a temporal resolution of 1 h. To align the sites to stable South America, sites on the rigid plate have to be selected ideally far away from the location of the Pisagua event. As a result of data gaps there are only a small number of sites matching



these requirements. Here only the stations in Arequipa, Peru (areq), and Cordoba, Argentina (unsa) cover the whole time span of processing. For the co-seismic displacements, exactly the same strategy as for the daily solutions was used. The displacements are the difference between the static coordinates from one day before and after the event, excluding data during the event.

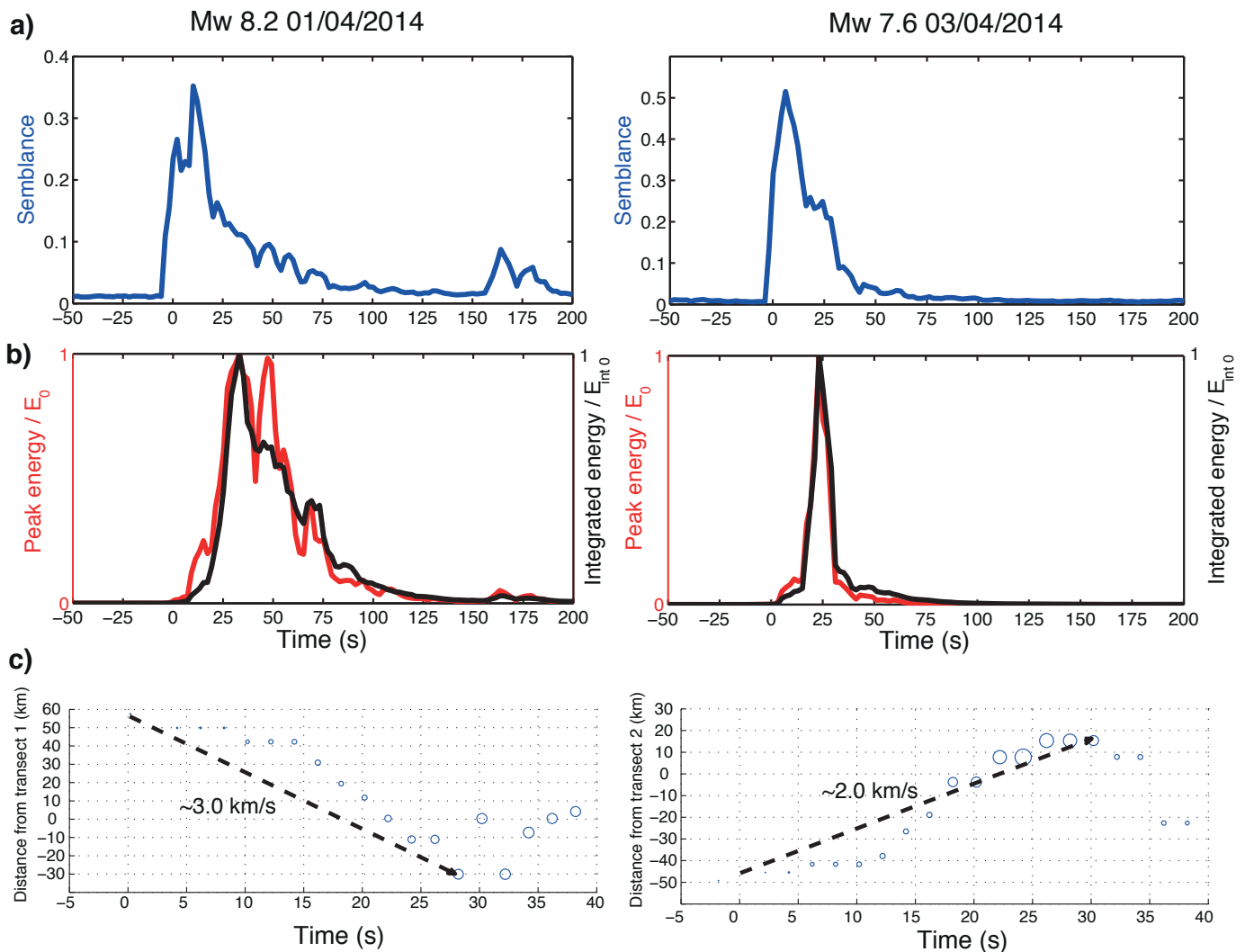
29. Zhang, Y. *et al.* The 2009 L'Aquila  $M_w$  6.3 earthquake: a new technique to locate the hypocentre in the joint inversion of earthquake rupture process. *Geophys. J. Int.* **191**, 1417–1426 (2012).
30. Hayes, G. P., Wald, D. J. & Johnson, R. L. Slab1.0: a three-dimensional model of global subduction zone geometries. *J. Geophys. Res.* **117**, 1–15 (2012).
31. Wang, R. A simple orthonormalization method for stable and efficient computation of Green's functions. *Bull. Seismol. Soc. Am.* **89**, 733–741 (1999).
32. Kennett, B. L. N., Engdahl, E. R. & Buland, R. Constraints on seismic velocities in the Earth from travel times. *Geophys. J. Int.* **122**, 108–124 (1995).
33. Bassin, C., Laske, G. & Masters, G. The current limits of resolution for surface wave tomography in North America. *Eos* **81**, F897 (2000).
34. Ishii, M., Shearer, P. M., Houston, H. & Vidale, J. E. Extent, duration and speed of the 2004 Sumatra–Andaman earthquake imaged by the Hi-Net array. *Nature* **435**, 933–936 (2005).
35. Neidell, N. & Taner, M. Semblance and other coherency measures for multichannel data. *Geophysics* **36**, 482–497 (1971).
36. Brooks, B. A. *et al.* Orogenic-wedge deformation and potential for great earthquakes in the central Andean backarc. *Nature Geosci.* **4**, 380–383 (2011).
37. Allmendinger, R. W., González, G., Yu, J., Hoke, G. & Isacks, B. Trench-parallel shortening in the Northern Chilean Forearc: tectonic and climatic implications. *Bull. Geol. Soc. Am.* **117**, 89 (2005).
38. Kennett, B. L. N. & Engdahl, E. R. Traveltimes for global earthquake location and phase identification. *Geophys. J. Int.* **105**, 429–465 (1991).
39. Wang, R., Lorenzo-Martin, F. & Roth, F. PSGRN/PSCMP—a new code for calculating co- and post-seismic deformation, geoid and gravity changes based on the viscoelastic–gravitational dislocation theory. *Comput. Geosci.* **32**, 527–541 (2006).
40. Menke, W. *Geophysical Data Analysis: Discrete Inverse Theory* (Academic, 2012).
41. Wdowinski, S., Bock, Y., Zhang, J., Fang, P. & Genrich, J. Southern California Permanent GPS Geodetic Array: spatial filtering of daily positions for estimating coseismic and postseismic displacements induced by the 1992 Landers earthquake. *J. Geophys. Res.* **102**, 57–70 (1997).
42. Husen, S., Kissling, E., Flueh, E. & Asch, G. Accurate hypocentre determination in the seismogenic zone of the subducting Nazca Plate in northern Chile using a combined on-/offshore network. *Geophys. J. Int.* **138**, 687–701 (1999).
43. Waldhauser, F. & Ellsworth, W. L. A double-difference earthquake location algorithm: method and application to the northern Hayward fault, California. *Bull. Seismol. Soc. Am.* **90**, 1353–1368 (2000).
44. Sippl, C. *et al.* Geometry of the Pamir–Hindu Kush intermediate-depth earthquake zone from local seismic data. *J. Geophys. Res. Solid Earth* **118**, 1438–1457 (2013).
45. Kagan, Y. Short-term properties of earthquake catalogs and models of earthquake source. *Bull. Seismol. Soc. Am.* **94**, 1207–1228 (2004).
46. Woessner, J. & Wiemer, S. Assessing the quality of earthquake catalogues: estimating the magnitude of completeness and its uncertainty. *Bull. Seismol. Soc. Am.* **95**, 684–698 (2005).
47. Helmstetter, A., Kagan, Y. & Jackson, D. Comparison of short-term and time-independent earthquake forecast models for southern California. *Bull. Seismol. Soc. Am.* **96**, 90–106 (2006).
48. Marzocchi, W. & Sandri, L. A review and new insights on the estimation of the  $b$ -value and its uncertainty. *Ann. Geophys.* **46**, 1271–1282 (2003).
49. Shi, Y. & Bolt, B. The standard error of the magnitude–frequency  $b$  value. *Bull. Seismol. Soc. Am.* **72**, 1677–1687 (1982).
50. Hainzl, S., Zakharova, O. & Marsan, D. Impact of aseismic transients on the estimation of aftershock productivity parameters. *Bull. Seismol. Soc. Am.* **103**, 1723–1732 (2013).
51. Habermann, R. E. in *Earthquake Prediction: An International Review* (eds Simpson, D. W. & Richards, P. G.) 29–42 (American Geophysical Union, 1981).
52. Dach, R., Hugentobler, U., Fridez, P. & Meindl, M. *Bernese GPS software version 5.0. User manual*, <<http://www.bernese.unibe.ch/docs50/DOCU50.pdf>> (Astronomical Institute, Univ. Bern, 2007).
53. Dach, R. *et al.* Improved antenna phase center models for GLONASS. *GPS Solut.* **15**, 49–65 (2011).
54. Letellier, T. *Étude des Ondes de Marée sur les Plateaux Continentaux*. Thesis, Univ. Toulouse III (2004).
55. Boehm, J., Niell, A., Tregoning, P. & Schuh, H. Global Mapping Function (GMF): a new empirical mapping function based on numerical weather model data. *Geophys. Res. Lett.* **33**, L07304 (2006).



**Extended Data Figure 1 | Slip inversion scenarios employing different data sets and final waveform fits.** **a**, Final slip distribution of the 1 April mainshock obtained from the waveform inversion (left) of the teleseismic and local strong-motion seismograms, the inversion (middle) of static GPS displacement data, and the joint inversion (right) of the waveform and GPS data. **b**, The same for the 3 April aftershock. **c**, Data fit of the joint kinematic inversion for the

1 April mainshock. Top: observed and modelled teleseismic P waveforms. Station codes are marked on the seismogram and on the map. Bottom: comparison between the observed and modelled local strong-motion waveforms. Traces are scaled to a common maximum in each sub-plot. **d**, The same for the 3 April aftershock.

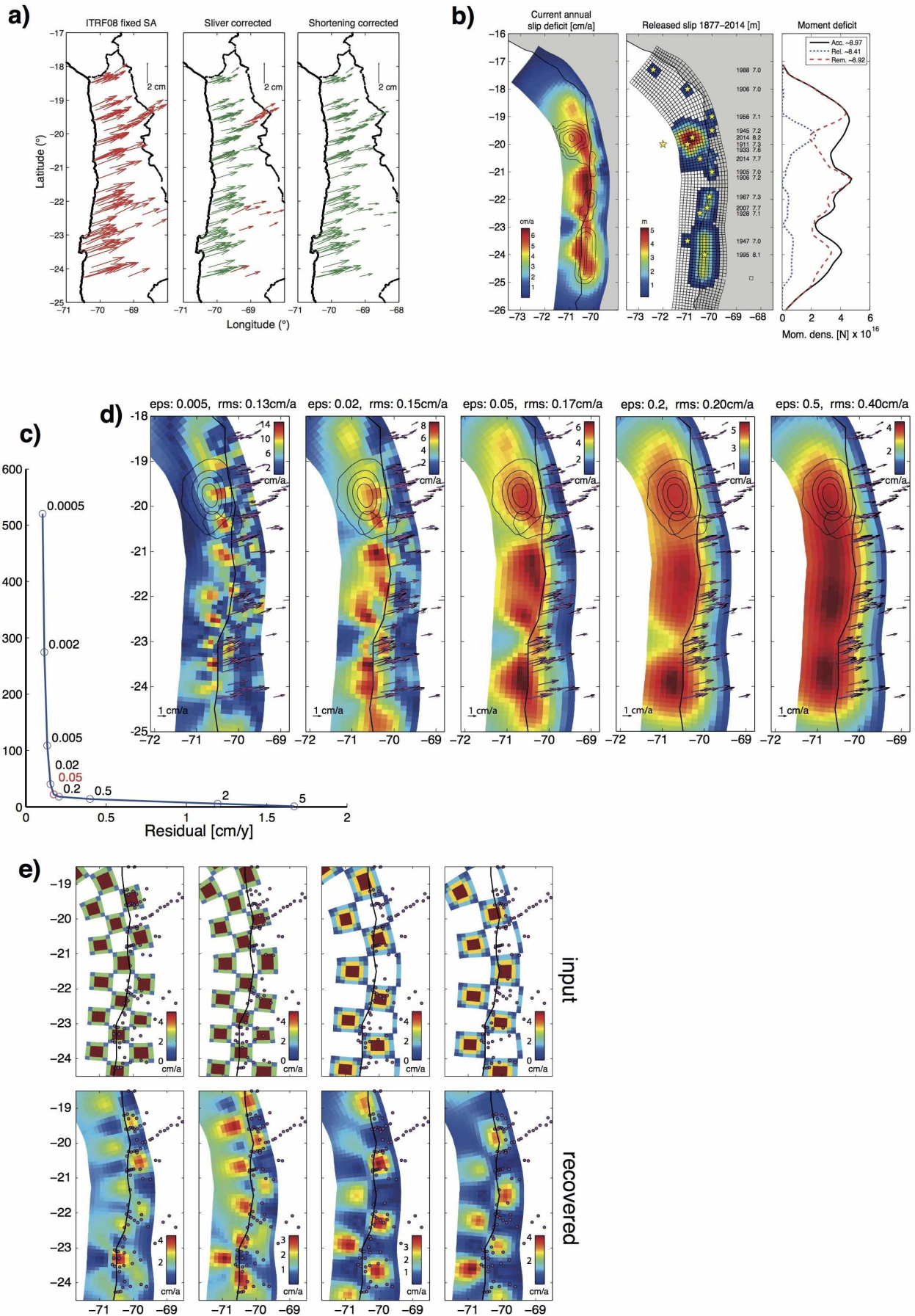




**Extended Data Figure 2 | Source time history and rupture velocity estimation from backprojection of high frequency teleseismic waves.**

**a, b,** Time history of the peak semblance at each time frame (blue) (**a**) and the corresponding energy (red, arbitrary units) for the mainshock (left) and the Iquique aftershock (right) (**b**). Energy integrated over the whole grid is plotted as a black line. Whereas the red curves describe the energy time history of one (the principal) radiating point, the black lines take into account the seismic energy emitted from the whole source area. The time axis represents the central point of the sliding windows 8 s long; that is, the first onset of the event will affect the energy and semblance at nominal times up to 4 s before the physical

onset of rupture. The semblance and energy peak at  $\sim 160$  s corresponds to an early aftershock. The area of the diamonds of Fig. 2b is scaled to the energy (red curves) shown in **b** (only solutions with semblance higher than 0.05 are shown in Fig. 2b). **c,** Distance of maximal semblance peaks to a reference profile (transects 1 and 2 for the mainshock (left) and the aftershock (right), respectively, plotted in Supplementary Videos 3 and 4). The figure is zoomed in the downdip migrations of the rupture fronts (about 0–30 s). The accelerated propagation can be identified in the interval 15–30 s. The area of the circles is scaled to the energy of the semblance maxima (red curves in **b**).

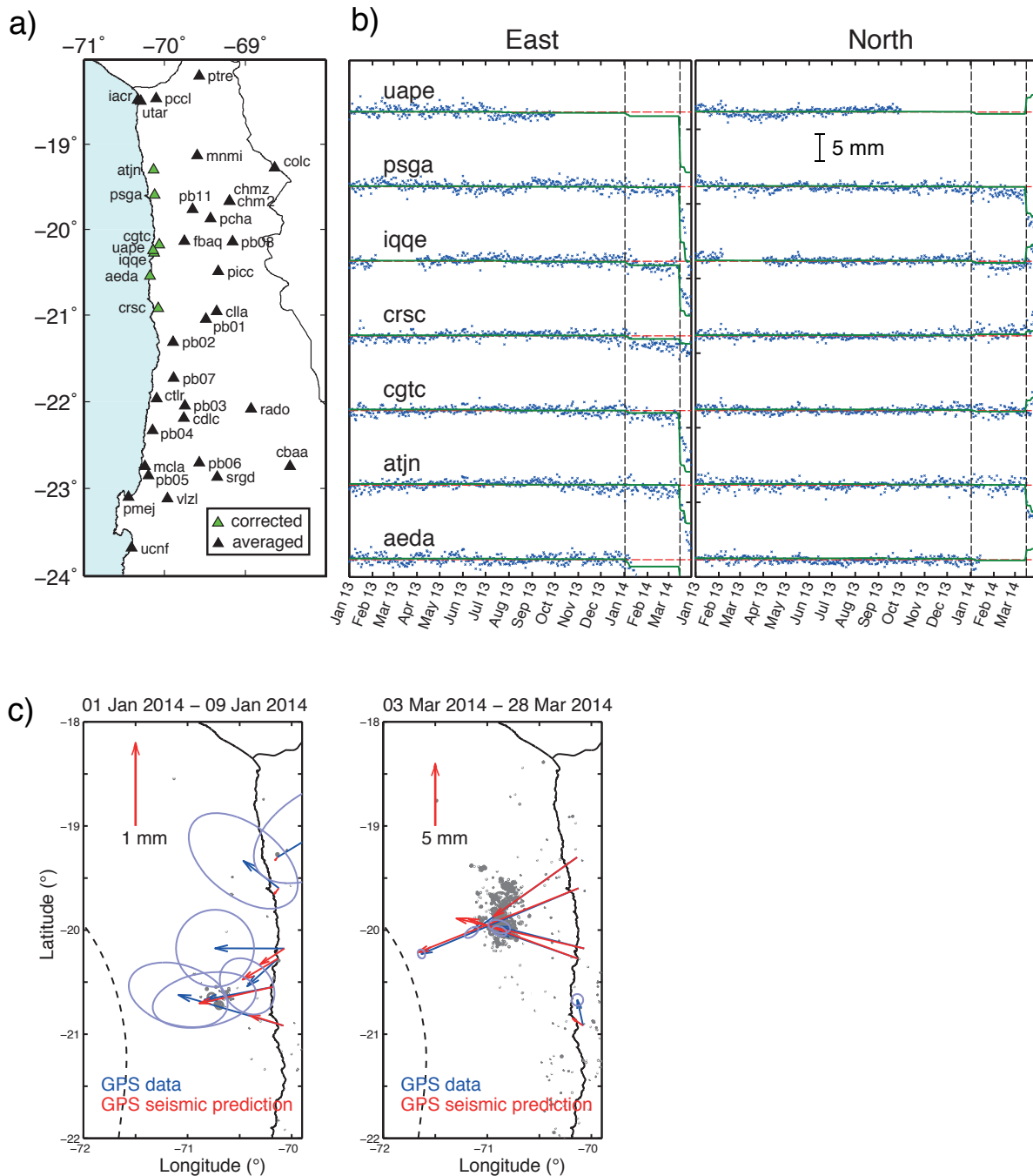


**Extended Data Figure 3 | Interseismic GPS data corrections, slip deficit estimation and sensitivity tests for interseismic locking inversion.**

**a**, Demonstration of the effect of sliver and shortening corrections on the interseismic GPS data. The left plot shows the data in the stable South American reference frame. Red vectors indicate the stations that the corrections were applied to. All stations underwent the sliver correction. Stations in the northeast and southeast underwent shortening corrections. **b**, Slip deficit estimation. The left panel shows our locking model; the central panel shows a compilation of events since 1877 according to ref. 1 plus the Antofagasta and Tocopilla earthquakes of 1995 and 2007 (refs 4, 7), as well as our solutions for the Pisagua mainshock and largest aftershock. The right panel shows moment density along the trench projected on latitude. The total accumulated moment corresponds to a  $M 8.97$  event. This is about one-sixth of the moment released during the 1960 Valdivia  $M 9.5$  event further south, but sixfold that released in our region of interest between 1877 and now according to the events listed

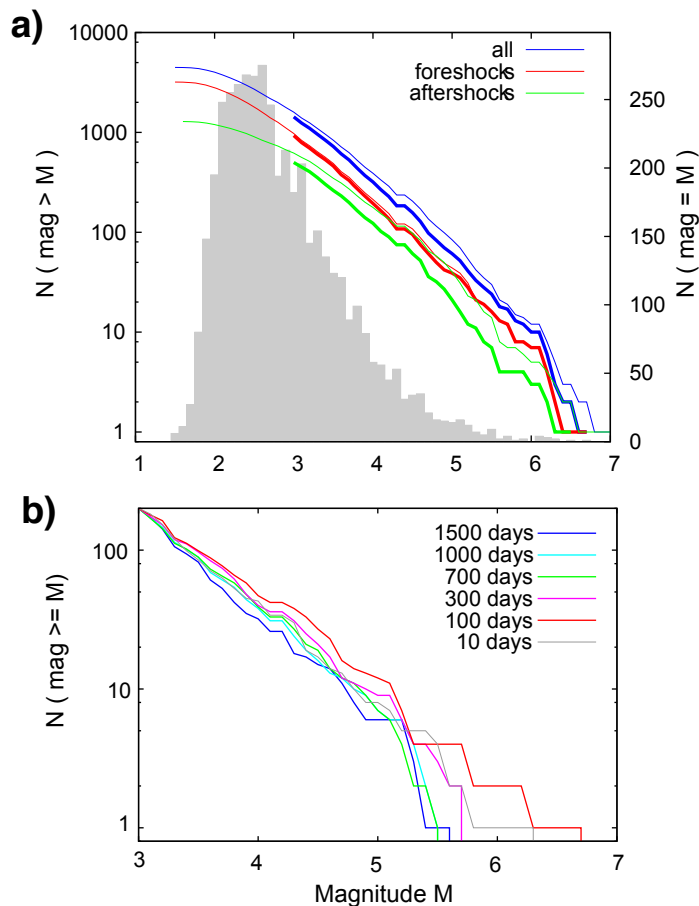
in the central panel summing to a magnitude of 8.41. Even though the Pisagua sequence released a significant amount of the moment in the northernmost part, the remaining moment would still correspond to  $M 8.92$ . **c**, Model smoothness plotted against residual. The optimal smoothing factor of 0.05 in the corner of the L-curve resulted in a residual of  $0.17 \text{ cm yr}^{-1}$ . **d**, A selection of solutions with different smoothing factors. The central solution is the one we prefer. Black lines are 1-m isolines of the co-seismic slip distribution of the mainshock and the largest aftershock. **e**, Checkerboard tests of locking. Top: forward models consisting of three and two rows of locked patches. Lower panels: inverted locking patterns using the signal from the forward models at the GPS station positions applying the same uncertainties as in the actual observation data. For three locking rows, the trenchward row is clearly missed, whereas the areas closer to the station positions (magenta) are captured fairly well, the resolution being about 40 km.





**Extended Data Figure 4 | Pre-seismic GPS displacement time series and maps.** **a**, Map showing stations used for common-mode filtering (black triangles) and those to which the correction signal is applied (green triangles). **b**, East and north displacement time series of the detrended, common-mode filtered data are plotted with blue crosses. The green lines are the cumulative GPS displacements predicted by the forward modelling of elastic displacements for events in the seismic foreshock catalogue. Black vertical dashed lines indicate the onsets of the two clusters of 2014. The red dashed line shows the zero positions of the GPS after detrending. A significant departure of the data from this zero position is an indication of transient motion at that station. **c**, The two panels show the GPS data displacements (blue) and the forward

modelled GPS displacements of the seismically related slip (red) during the periods shown above each panel. Both the data and the predictions have been smoothed with a nine-day moving-average filter. Error ellipses are shown for the data displacements. The black dashed line is the trench and the solid black lines are the coastline and political borders. Events from the foreshock catalogue for days within the specified periods (also considering length of smoothing window) are plotted in dark grey. For the first 2014 cluster (left panel), GPS stations of interest in the south move towards a common source. For the second 2014 cluster (right panel), GPS vectors point towards the eventual  $M_w$  8.1 rupture zone.



**Extended Data Figure 5 | Magnitude histogram of analysed catalogue and frequency-magnitude distributions for different data subsets.** **a**, Frequency-magnitude distribution of earthquakes within latitude  $17.0^\circ$ – $21.0^\circ$  S and longitude  $70.0^\circ$ – $72.0^\circ$  W, used in our  $b$ -value analysis and ETAS modelling. The histogram of the overall seismicity is shown by grey boxes, and thin lines refer to the cumulative distributions of foreshocks, aftershocks and the overall activity. Bold lines refer to the data used for the analysis above the magnitude threshold ( $M_c = 3$ ) ignoring periods of incomplete recordings after larger earthquakes. **b**, Frequency-magnitude distributions at different times before the mainshock. The distributions correspond to the  $b$  values shown in grey in Fig. 3e.